High internal inductance for steady-state operation in ITER and a reactor

J.R. Ferron[1], C.T. Holcomb[2], T.C. Luce[1], J.M. Park[3], E. Kolemen[4], R.J. La Haye[1], W.M. Solomon[4] and F. Turco[5]

[1] General Atomics, PO Box 85608, San Diego, CA 92186-5608, USA
[2] Lawrence Livermore National Laboratory, 7000 East Ave, Livermore, CA 94550, USA
[3] Oak Ridge National Laboratory, PO Box 2008, Oak Ridge, TN 37831, USA
[4] Princeton Plasma Physics Laboratory, PO Box 451, Princeton, NJ 08543-0451, USA
[5] Columbia University, 2960 Broadway, New York, NY 10027-6900, USA

E-mail: ferron@fusion.gat.com

CrossMark

Abstract

Increased confinement and ideal stability limits at relatively high values of the internal inductance (ℓ_i) have enabled an attractive scenario for steady-state tokamak operation to be demonstrated in DIII-D. Normalized plasma pressure in the range appropriate for a reactor has been achieved in high elongation and triangularity double-null divertor discharges with $\beta_N \approx 5$ at $\ell_i \approx 1.3$, near the ideal $n = 1$ kink stability limit calculated without the effect of a stabilizing vacuum vessel wall, with the ideal-wall limit still higher at $\beta_N > 5.5$. Confinement is above the H-mode level with $H_{98(y,2)} \approx 1.8$. At $q_{95} \approx 7.5$, the current is overdriven, with bootstrap current fraction $f_{BS} \approx 0.8$, noninductive current fraction $f_{NI} > 1$ and negative surface voltage. For ITER (which has a single-null divertor shape), operation at $\ell_i \approx 1$ is a promising option with $f_{BS} \approx 0.5$ and the remaining current driven externally near the axis where the electron cyclotron current drive efficiency is high. This scenario has been tested in the ITER shape in DIII-D at $q_{95} = 4.8$, so far reaching $f_{NI} = 0.7$ and $f_{BS} = 0.4$ at $\beta_N \approx 3.5$ with performance appropriate for the ITER Q=5 mission, $H_{89}\beta_N/q_{95}^2 \approx 0.3$. Modeling studies explored how increased current drive power for DIII-D could be applied to maintain a stationary, fully noninductive high ℓ_i discharge. Stable solutions in the double-null shape are found without the vacuum vessel wall at $\beta_N = 4$, $\ell_i = 1.07$ and $f_{BS} = 0.5$, and at $\beta_N = 5$ with the vacuum vessel wall.

Keywords: internal inductance, steady-state, tokamak operation

(Some figures may appear in colour only in the online journal)

1. Introduction

A tokamak discharge with a relatively high value of the internal inductance, $\ell_i > 1$, has advantages that make it attractive for steady-state operation at high normalized pressure (β_N). Both confinement and the stability limit to β_N have been demonstrated in previous experiments to improve as ℓ_i increases [1–12]. The energy confinement time normalized to a scaling law, for instance H_{89} [13], was increased a factor of two or more by increasing ℓ_i, and β_N as high as 6 was achieved. These discharge performance improvements arise largely as a result of higher poloidal field in the discharge

core and larger magnetic shear in the outer half of the plasma when the current density profile is more peaked. Plasmas with high ℓ_i and $\beta_N \approx 4$–5 are predicted by theory to be stable to low toroidal mode number (n) ideal MHD instabilities even without the effect of a conducting vacuum vessel wall [14, 15]. In addition, the β_N limit as determined by the infinite-n ballooning mode is expected to increase with ℓ_i [16]. These features make a high ℓ_i discharge a candidate for a reactor that could either operate stably at $\beta_N \approx 4$ without the requirement for a nearby conducting wall or $n \geqslant 1$ active stabilization coils, or at $\beta_N \approx 5$ with wall stabilization. This is the range of β_N envisioned in reactor studies such as ARIES-AT [17].

Here, $\beta_N = 100\beta_T a B_T / I_p$ and $\ell_i = \int dV B_P^2/V/(\oint B_P dl/\oint dl)^2$. $\beta_T = 2\mu_0 \langle P \rangle / B_T^2$, $\langle P \rangle$ is the volume average plasma pressure, I_p (MA) is the plasma current, a (m) is the minor radius, B_T (T) is the toroidal magnetic field, B_P (T) is the poloidal magnetic field, V (m^3) is the plasma volume and the path for the line integrals is the plasma boundary.

Steady-state tokamak operation is optimum with a high fraction of bootstrap-driven current (f_{BS}), but typical bootstrap current density (J_{BS}) profiles can have limited compatibility with an elevated value of ℓ_i. The dependence of the stability limit to β_N on ℓ_i strengthens as the core pressure profile is broadened [14] and stability limits are highest with high plasma elongation κ and triangularity [15, 18]. A broad core pressure profile and strong discharge shaping both increase J_{BS} in the outer half of the plasma. As the fraction of I_p resulting from bootstrap current in the outer half of the plasma increases, the maximum value of ℓ_i that can be obtained by tailoring the profile of the externally-driven current density will decrease. Taking this into account, a proposal was made in [15] for an 'optimized high ℓ_i' discharge scenario where there is a compromise between high ℓ_i and high f_{BS}: $\ell_i \approx 1$, $\beta_N = 3.5$–4.0, and $f_{BS} \approx 0.5$. About half of the current would be provided by externally-driven current near the axis. Although the total amount of externally-driven current would be larger than in a low ℓ_i, high q_{min} steady-state scenario, where f_{BS} is conceptually (e.g. [17]) above 0.8, the required external current drive power could be comparable because of increased efficiency for external current drive near the axis.

The maximum achievable ℓ_i in a high β_N, H-mode discharge is strongly dependent on the parameters of the H-mode pressure pedestal because a large fraction of the bootstrap-driven current is a result of the steep pressure gradient there. Therefore, a discharge scenario with increased ℓ_i would be particularly applicable under conditions with reduced pedestal height resulting from pedestal physics and/or stabilization of edge-localized modes (ELMs) using 3D fields. Because of the requirement to mitigate the effect of ELMs, and the planned availability of neutral beam and electron cyclotron power sources appropriate for near-axis current drive, a high ℓ_i regime is a possibility for the steady-state mission in ITER. The reduced global confinement at low pedestal pressure could be compensated by increased core confinement when the reduced J_{BS} in the pedestal is replaced by increased current density in the discharge core. The increase in ℓ_i could also increase the β_N limit, but the more peaked core pressure profile resulting from the reduction in pedestal pressure would tend to offset this change.

This paper presents progress in DIII-D experiments on the assessment of the potential of the high ℓ_i scenario for steady-state operation. A method to access a high ℓ_i current density profile without the rapid current ramp or discharge shape change that has been used in previous experiments is described in section 2. The capability to produce a high f_{BS}, $\beta_N \approx 5$ discharge in H-mode is discussed in section 3. In discharges with the scaled ITER shape, the optimized $\ell_i \approx 1$ scenario has been tested along with the effect of a reduction in the H-mode pedestal height (section 4). The calculated β_N limits
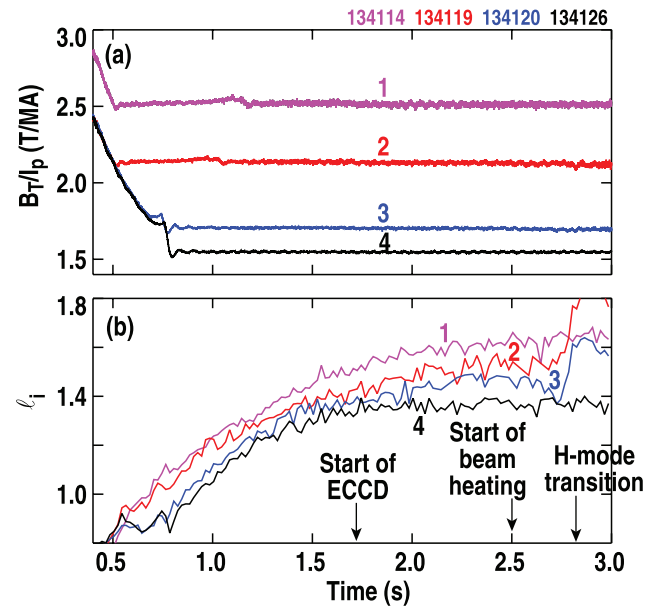

Figure 1. Formation of the initial equilibrium with a high value of ℓ_i. (*a*) $B_T/I_p \sim q_{95}$ and (*b*) internal inductance. During the ohmic phase of the discharge, the electron density $n_e \approx 2.5 \times 10^{19}$ m^{-3}.

of these discharges are presented in section 5. Access to high β_N values is shown to result from a self-consistent broadening of the pressure profile as well as the increase in ℓ_i. Modeling used to project parameters for stationary, high ℓ_i, fully non-inductive operation in DIII-D is described in section 6 along with an analysis of the effect of changes in the pedestal current density. The conclusions are presented in section 7.

2. Discharge formation

The high ℓ_i, high β_N discharges described here have not yet been operated with a stationary current density (J) profile as sufficient externally-driven current is not yet available. These discharges do, though, allow the study of the capability to access the discharge parameter range envisioned for future steady state operation. The high β_N equilibrium is formed by beginning the discharge with an initial, low β_N phase [6] with only inductive heating so that the electron temperature (T_e) is low and the characteristic timescale [19] for relaxation of the J profile, $\tau_R \approx 0.2$ s, is short. The discharge remains in these conditions long enough for the current profile to evolve to a stationary state (figure 1). Because the conductivity is very low in the outer half of the plasma, the current density profile becomes peaked in the core and ℓ_i reaches a relatively large asymptotic value.

The asymptotic value of ℓ_i scales with $q_{95} \sim B_T/I_p$ (figure 1) as a result of constraints on the minimum value of q (q_{min}). The minimum possible $q(0)$ (maximum $J(0)$) is desirable in order to maximize ℓ_i, but the onset of sawtooth oscillations maintains $q(0) \approx 1$ and limits B_T/J near the axis. Thus, as I_p increases, the core J peak broadens, forming a somewhat step-like profile (figure 2). The width of the core J peak will be larger as I_p increases at fixed B_T, resulting in lower ℓ_i. The value of B_T/I_p is used here for comparison because q_{95} varies
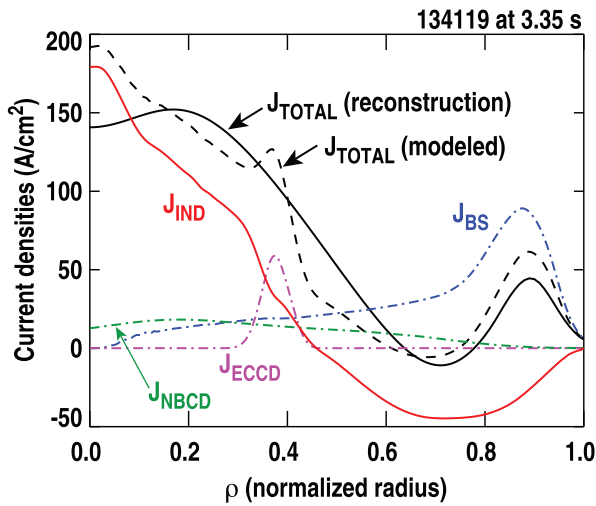
Figure 2. Current density profiles at 3.35 s during the discharge shown in figures 3(a)–(c). The total J is shown from two sources. Solid line: obtained from an equilibrium reconstruction using experimental data and $C_{BS} = 0.8$, dashed line: calculated using the ONETWO transport code [25]. The individual current density components were also calculated using ONETWO: bootstrap J_{BS}, neutral-beam-driven J_{NBCD}, electron-cyclotron-driven J_{ECCD}, and inductively driven J_{IND}.

significantly as β_N increases as a result of changes in the shape of the q profile near the plasma boundary. For the discharges shown in figure 1, during the ohmic phase q_{95} is between 3.75 and 6.8, while at the time of the peak β_N, $q_{95} = 4.7$–9.8.

After the asymptotic value of ℓ_i is reached ($t = 1.7$ s), electron cyclotron current drive (ECCD) is added near $\rho \approx 0.4$ to add externally-driven current J_{ECCD} at the edge of the core peak (figure 2) and to increase T_e. The increase in T_e results in a factor of ≈ 10 increase in τ_R so that the core inductive current density (J_{IND}) peak is essentially 'frozen' in place, evolving only very slowly for the remainder of the discharge. As discussed in section 5, the transition into H-mode occurs either at 2.8 s after the neutral beam heating begins at 2.5 s (e.g. the discharge shown in figures 3(a)–(c), discussed in section 3) or at 1.9 s during the phase with only ECCD heating (e.g. figure 7, section 4). For the discharges discussed here, all of the neutral beams are injected in the direction of the plasma current.

This method to produce a high ℓ_i, high β_N plasma is potentially useful for a burning plasma device because it is relatively simple. There is no requirement for rapid changes in I_p, elongation or radius as used in the past to increase ℓ_i [1, 8, 10], techniques which would be difficult to implement in a large, superconducting device and which would impose restrictions on the initial flattop value of I_p. The method does not require formation of a diverted plasma shape, application of external heating sources, a transition into H-mode, or feedback control of the q profile during the I_p rampup, techniques that are used to form a target plasma with elevated q_{min} in current steady-state scenario experiments [20, 21]. Because there would be a long phase with relatively low T_e prior to initial application of the external heating, though, there could be an issue with the amount of flux required from the inductive heating coil. Also,
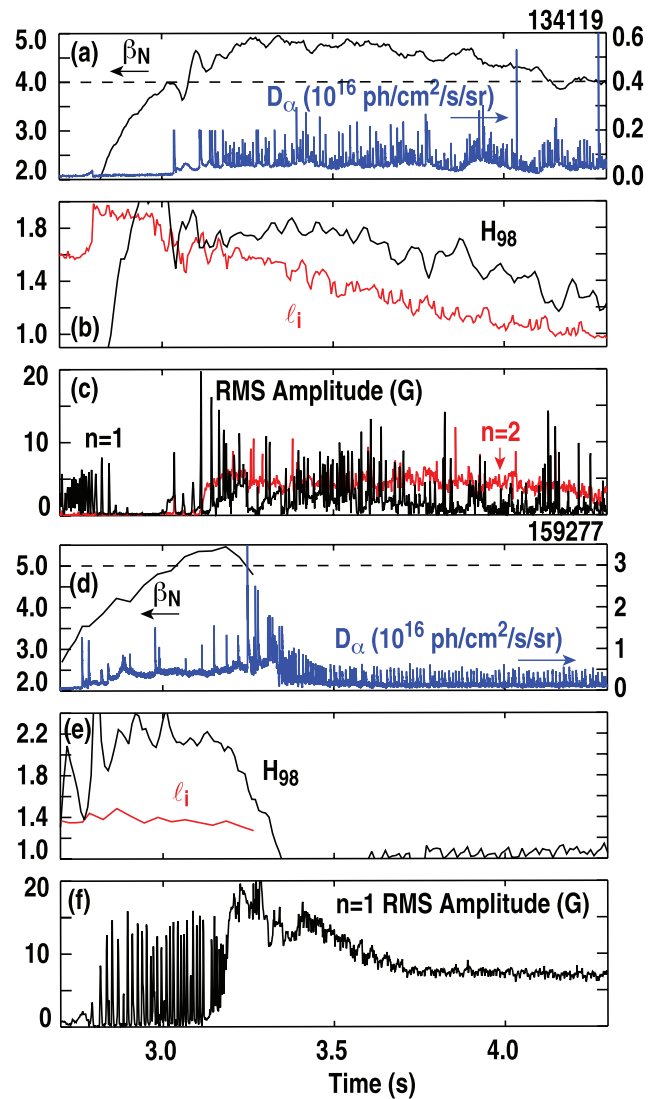

Figure 3. Time evolution of parameters in two high ℓ_i discharges with high β_N. A discharge with β_N sustained above 4: (a) β_N and divertor-region D_α, (b) ℓ_i and $H_{98(y,2)}$, (c) the amplitude of $n = 1$ and $n = 2$ poloidal field fluctuations. $n_e \approx 5.5 \times 10^{19}$ m^{-3} at $t = 3.1$ s dropping to $n_e \approx 4.5 \times 10^{19}$ m^{-3} by $t = 4.3$ s. A discharge that has β_N exceeding 5 for a short interval: (d) β_N and divertor-region D_α, (e) ℓ_i and $H_{98(y,2)}$, (f) the amplitude of $n = 1$ poloidal field fluctuations. $n_e \approx 6.7 \times 10^{19}$ m^{-3} at the peak β_N. $B_T = 1.7$ T, $I_p = 0.8$ MA in both cases.

the poloidal field system would need to be able to maintain vertical stability at the desired value of ℓ_i [22]. For instance, in ITER the vertical stability system is limited to $\ell_i \approx 1.2$ [23], sufficient for the 'optimized high ℓ_i' scenario discussed in section 1.

## 3. High bootstrap current fraction, high β_N double-null divertor discharges

In a double-null divertor configuration, discharges have been produced with β_N in the range required for a high power density reactor. An example is the discharge shown in figures 3(a)–(c) where $\beta_N \approx 4.8$ for 0.4 s, dropping slowly as ℓ_i decreases from
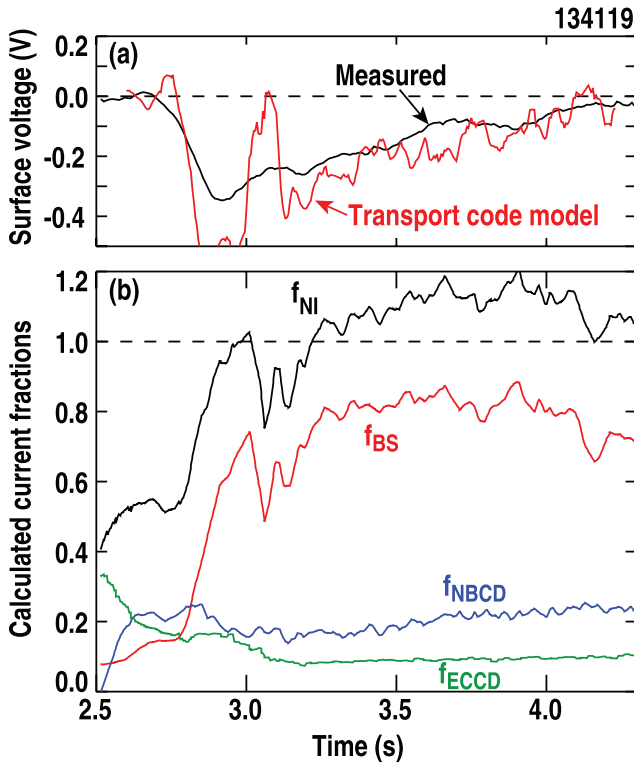
Figure 4. Parameters for the discharge shown in figures 3(*a*)–(*c*). (*a*) Measured and transport-code-calculated surface voltage, (*b*) noninductive current fraction (f_{NI}), bootstrap current fraction (f_{BS}), fraction of neutral-beam-driven current (f_{NBCD}), and fraction of ECCD current (f_{ECCD}).

an initial value of ≈ 1.6 to about 1.0. $\beta_N > 4$ is maintained for 1 s ($\approx 0.5\tau_R$) during a period with frequent ELMs, with excellent confinement, $H_{98(y,2)} \approx 1.8$ and $H_{89} \approx 2.6$ (where $H_{98(y,2)}$ is the H-mode confinement scaling law [24]). The decrease in β_N with time occurs because of the decrease in confinement as ℓ_i decreases with constant neutral beam power ≈ 11.8 MW and ECCD power ≈ 3 MW. $\beta_N > 5$ has been accessed briefly, as illustrated by the example in figures 3(*d*)–(*f*). In this case, β_N reaches 5 with normalized confinement above twice the prediction of scaling laws for H-mode as a result of the low ELM frequency just after the transition to H-mode and the increased $\ell_i \approx 1.3$. The β_N decreases as a result of strongly reduced confinement that begins at the onset of a continuous poloidal mode number $m = 2$, toroidal mode number $n = 1$ instability (section 5).

These discharges have a large fraction of the current driven noninductively as a result [21] of the high β_N and the relatively large $q_{95} \approx 7.5$ ($B_T/I_p = 2.1$). The total calculated noninductively driven current in the figures 3(*a*)–(*c*) discharge (figure 4(*b*)) exceeds the total plasma current as regulated using the inductive heating coil. This is primarily because of the high $f_{BS} \approx 0.8$, with the neutral-beam-driven current fraction $f_{NBCD} \approx 0.2$ and the ECCD current fraction $f_{ECCD} \approx 0.1$. A negative surface voltage (figure 4(*a*)) is required in order for the control system to maintain the target value of I_p with this large noninductively driven current combined with the inductively driven current density near the axis. A transport code simulation of the discharge predicts surface voltage that is close to, but slightly more
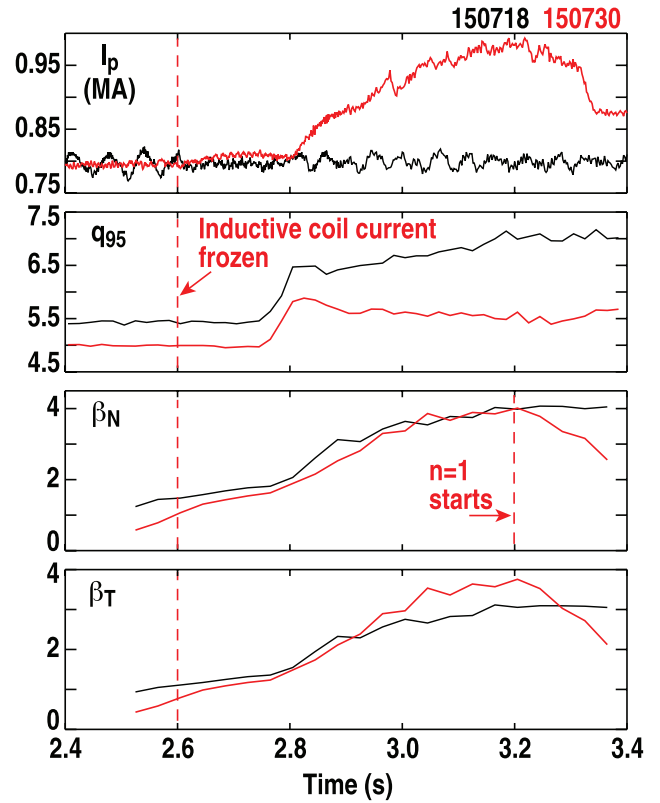
Figure 5. Parameters in two discharges that were formed similarly except that for the discharge shown in red, the current in the inductive heating coil was held fixed beginning at 2.6 s. During that discharge, a continuous $n = 1$ tearing mode began at 3.2 s, causing a decrease in β_N.
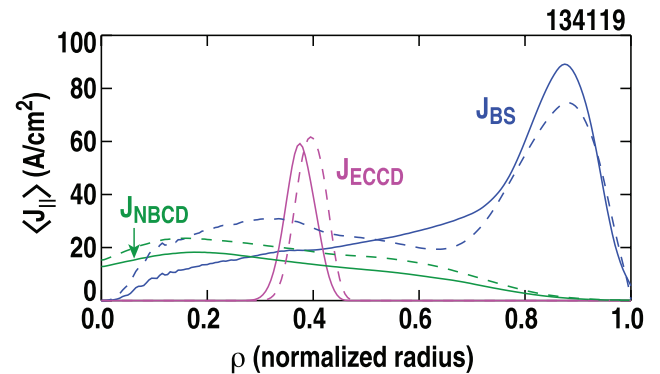
Figure 6. Noninductive current density profiles at 3.35 s (solid curves) and 4.1 s (dashed curves) during the discharge shown in figures 3(*a*)–(*c*). Here, $\langle\rangle$ indicates flux surface average.

negative, than the measurement (figure 4(*a*)). This indicates that the model somewhat over predicts the total noninductively driven current and/or the core-trapped inductively driven current. The current overdrive was confirmed through an increase in the total plasma current when the inductive coil current was held constant. An example is shown in figure 5 where, for the discharge shown in red, the inductive coil current was held fixed beginning at 2.6 s, resulting in an increase in the total current as β_N increased, a decrease in q_{95}, and access to higher β_T.

The current density components and the modeled surface voltage (figures 2, 4 and 6) were obtained using the ONETWO

[25] transport code. The code was provided as input an initial equilibrium reconstructed [26] using magnetic and motional Stark effect diagnostic measurements at 2.5 s, along with a time series of measured temperature and density profiles. Beginning with the initial equilibrium, the evolution of the current density profile was calculated from a time-dependent simulation of the poloidal flux diffusion using models for conductivity and J_{BS} [27, 28], J_{NBCD} (NUBEAM [29]) and J_{ECCD} (TORAY-GA [30]).

The peak in J_{BS} in the H-mode pedestal region is relatively high and broad (figure 2) as a result of the high values of β_N and $\beta_P \lesssim 3.4$, so it accounts for a significant amount of off-axis current. The transport-code-calculated total bootstrap current located in the pedestal region is 25–30% of I_p. In addition, the pedestal-region peak in J_{BS} extends well inside the inner boundary of the pedestal at $\rho \approx 0.84$ as a result of the broad core pressure profile (section 5). Thus the bootstrap current profile plays a strong role in determining the value of ℓ_i. Here, the pedestal region width is defined using the hyperbolic tangent fitting function [31].

The simulation of the current density profile evolution shows, though, that the time evolution of ℓ_i in these experiments is primarily determined by the time dependence of the toroidal electric field profile. f_{BS} remains roughly constant during the high β_N phase of the discharge, with only a small shift of J_{BS} from the H-mode pedestal region to the discharge core with time (figure 6) as β_N decreases and the pressure profile becomes more peaked (section 5). This change would tend to increase ℓ_i. Similarly, J_{NBCD} increases near the axis as a result of decreasing electron density, while there is little change in the J_{ECCD} profile. The negative surface voltage, though, penetrates relatively quickly through the outer half of the discharge, so that the calculated inductive electric field is zero at $\rho = 0.5$ by the time β_N reaches its peak value (as indicated by J_{IND} in figure 2). The negative inductively-driven current density in the outer half of the discharge offsets some of the bootstrap current, helping to maintain the elevated value of ℓ_i. The negative electric field penetrates slowly toward the axis during the high β_N phase, with the modeled field reaching zero at $\rho = 0.4$ by 3.8 s, and remaining positive, but gradually decreasing, in the region $\rho < 0.3$. The decreasing J_{IND} in the region near the axis results in the slow decrease in ℓ_i. With a long enough pulse duration, the discharge would eventually evolve toward a stationary state with a uniform toroidal electric field profile and a relatively low ℓ_i because of the off-axis bootstrap current. With additional current drive power, the portion of the evolving core J_{IND} profile driven by the positive electric field could be replaced with stationary profiles of J_{NBCD} and J_{ECCD} in order to maintain $\ell_i > 1$. The discharge would be operated at lower q_{95} in order to eliminate the noninductive current overdrive and set $f_{NI} = 1$ (section 6).

4. Discharges in the ITER scaled shape

The potential compatibility of the optimized $\ell_i \approx 1$, $f_{BS} \approx 0.5$ scenario [15] with ITER motivated studies of this type of discharge in the planned ITER shape, scaled to fit into the DIII-D
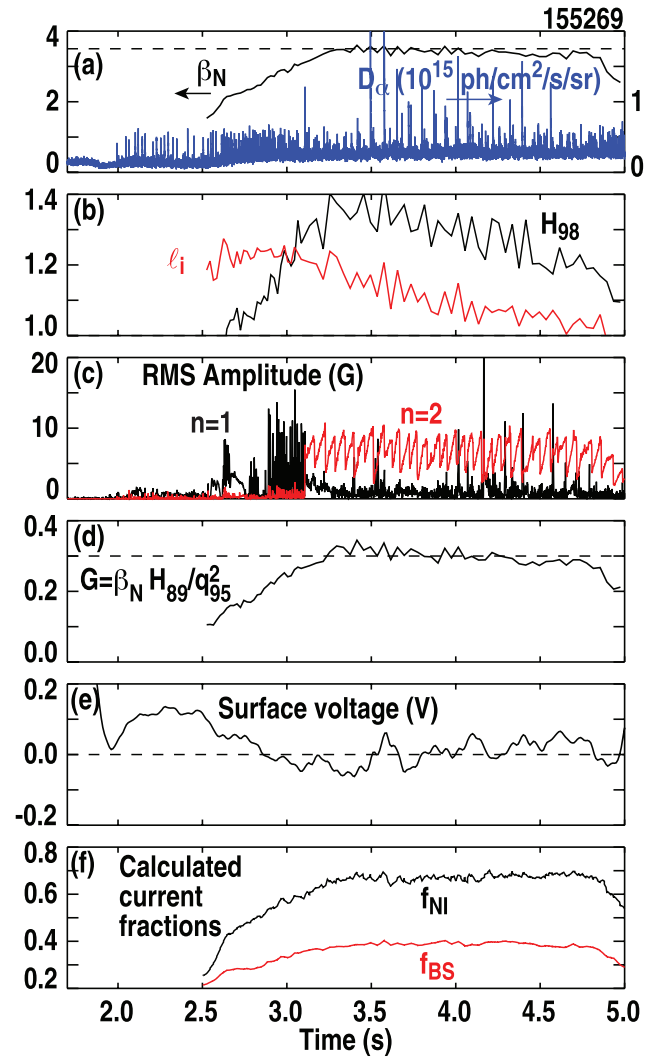
Figure 7. Parameters in a discharge operated in the ITER scaled shape. (*a*) β_N and divertor-region D_α, (*b*) internal inductance and normalized confinement, (*c*) amplitude of $n = 1$ and $n = 2$ poloidal field fluctuations, (*d*) the fusion gain factor, (*e*) the measured surface voltage, and (*f*) the noninductive and bootstrap current fractions. $B_T = 1.7$ T, $I_p = 0.92$ MA.

vacuum vessel. A high ℓ_i scenario is a possibility for ITER in the event that the H-mode pedestal pressure is found to be too low to achieve the target fusion gain for the steady-state mission in the high $q_{min} \approx 2$, relatively low $\ell_i < 0.8$ scenario [32]. ELM mitigation using 3D magnetic fields, for instance, can reduce the pedestal density and pressure. A reduction in the pedestal pressure reduces J_{BS} near the plasma boundary, leading naturally to increased ℓ_i.

With $q_{95} = 4.8$, near the value envisioned for steady-state operation in ITER [32], the experiment has thus far operated with $f_{NI} \approx 0.7$, $f_{BS} \approx 0.4$ and $\beta_N \approx 3.5$ (figures 7(*a*) and (*f*)). The initial $\ell_i \approx 1.25$ is lower than in the figure 3 discharges (figure 7(*b*)) as a result of the reduction in q_{95}. However, ℓ_i is still ≈ 1 at the end of the discharge because of reduced total bootstrap current in the H-mode pedestal region. In this discharge, the bootstrap current in the pedestal region accounts for ≈ 12% of the total current. The pedestal bootstrap current fraction is lower than in the case of the double-null divertor
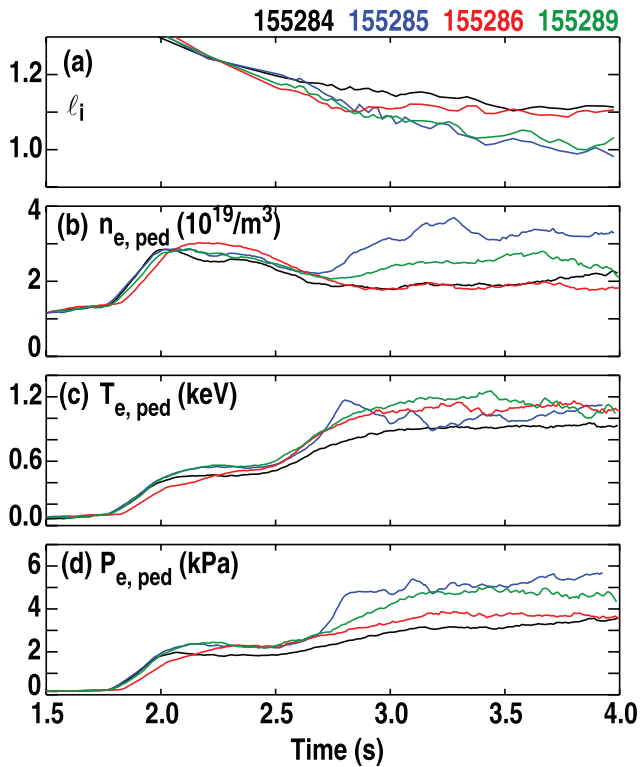
Figure 8. Time evolution of parameters in discharges produced in the scaled ITER shape with $q_{95} = 5.5$, $\beta_N = 3$, three of which have I coil current applied in an $n = 3$ configuration beginning at 2.1 s. Blue curves: no I coil current; green curves: 2 kA coil current in both coil rows with even parity, red curves: 5.5 kA in both coil rows with even parity; black curves: 5.5 kA, in the lower I coil row only. (*a*) Internal inductance. Parameters at the top of the H-mode pedestal: (*b*) electron density, (*c*) electron temperature, (*d*) electron pressure.

discharge (section 3) as a result of the change to the single-null divertor shape, the reduced q_{95}, and the lower β_N that results in reduced H-mode pedestal pressure. The pedestal pressure is only two thirds of the pressure in the double-null divertor discharge even though I_p is about 12% higher. Discharge performance is close to the estimated requirement for the ITER steady-state mission with $G = \beta_N H_{89}/q_{95}^2 \approx 0.3$ (figure 7(*d*)). During the initial portion of the high β_N phase, the sum of the inductive current density near the axis and the noninductively driven current is large enough that the surface voltage is near zero (figure 7(*e*)).

The effect of a reduction in the H-mode pedestal pressure on the current density profile was tested by applying $n = 3$ fields from the DIII-D internal non-axisymmetric coils, the I coils [33]. Four discharges (figure 8) were run identically until the I coil current was turned on at 2.1 s. With the I coil current, the pedestal electron density, temperature and pressure decreased as the strength of the $n = 3$ field was increased (figures 8(*b*)–(*d*)). As anticipated, the corresponding modifications to the current density profile resulted in evolution to a higher value of ℓ_i in the discharges with the lower pedestal pressure (figures 8(*a*) and 9). The increase in the average value of ℓ_i during the high β_N phase corresponds well with a factor of two decrease in the fraction of I_p supplied by bootstrap current
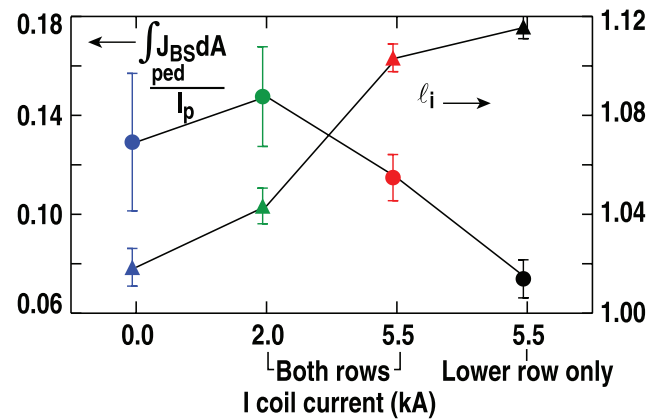

Figure 9. Parameters averaged over the interval 3–4 s for the discharges shown in figure 8. Circles: fraction of I_p that is provided by bootstrap current located in the H-mode pedestal region (as defined by the fit of the electron pressure profile to a hyperbolic tangent function [31]). The bootstrap current fraction was determined by integrating J_{BS} as calculated from the model [27, 28] over the region of the pedestal. Triangles: ℓ_i. The error bars show the standard deviation. The data point colors match the colors of the curves in figure 8.

located in the pedestal region (figure 9). Addition of the $n = 3$ field also resulted in a peaking of the pressure profile, and thus an increase in J_{BS} in the region between the pedestal and the axis, contributing to the increase in ℓ_i.

5. Stability limits to β_N

Global, ideal MHD, low n instabilities are expected to set the ultimate limit to pressure, but, as discussed in this section, this type of mode is not observed to directly determine the β_N that is actually achieved. The high values of β_N attained at high ℓ_i are close to, but below, the calculated limits set by the ideal $n = 1$ kink and the ideal infinite-n ballooning instabilities. The long-duration double-null discharge (figures 3(*a*)–(*c*)), for instance, had peak performance, $\beta_N \approx 4.8$, near the no-wall limit with the ideal-wall limit higher at $\beta_N \approx 5$–6 (figure 10(*a*)). The ballooning mode stability limit is slightly below that of the ideal-wall $n = 1$ mode. Consistent with these stability calculations, a global, pressure-limiting instability has not yet been clearly observed in the experiment. Instead, in the cases where stability determines the limit to performance, the observed mode is most commonly an $m = 2/n = 1$ resistive tearing mode. The duration at $\beta_N > 5$ was limited by a 2/1 mode in the double-null shape discharge in figures 3(*d*)–(*f*). In the ITER scaled shape (figure 7), the value of β_N that could be sustained for the full discharge duration was limited by the 2/1 resistive mode to a value below the no-wall ideal limit (figure 10(*b*)).

There is uncertainty in the size of the gap between the experimental β_N and the calculated ideal $n = 1$ stability limit that arises from sensitivity of the stability limit calculation to the current density profile in the H-mode pedestal region and the lack of diagnostics that provide a local measurement of the current density there. In order to estimate the β_N at the stability limit, test equilibria were produced using
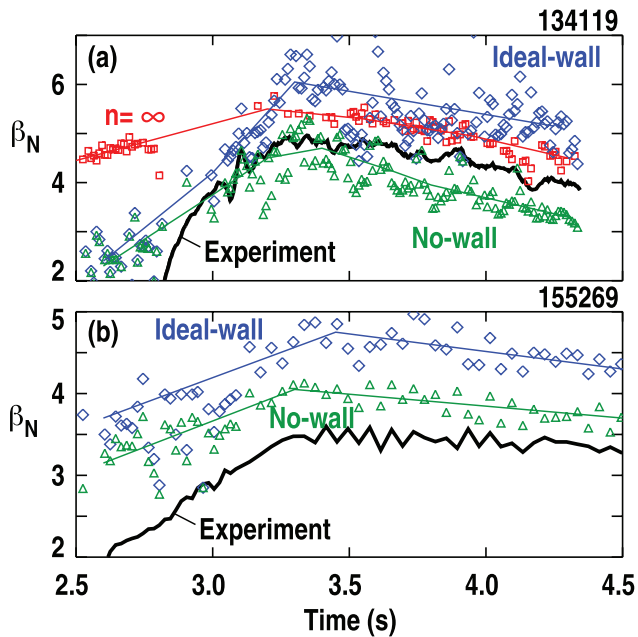
Figure 10. Ideal MHD $n = 1$ stability limits calculated without including the effect of the conducting vacuum vessel wall (triangles) and including the wall (diamonds). (*a*) Double-null divertor shape discharge shown in figures 3(*a*)–(*c*). Here the squares are the ideal infinite-*n* ballooning mode stability limit calculated using the BALOO code [34]. (*b*) ITER shape discharge shown in figure 7. In the equilibrium reconstruction for the double-null shape, the pedestal current density was constrained to the model-predicted J_{BS} scaled by the factor $C_{BS} = 0.8$ plus the full, model-predicted J_{IND}. $C_{BS} = 0.8$ minimizes χ^2 during most of the high β_N phase of this discharge. In the equilibrium reconstructions for the ITER shape discharge, the full model-predicted J in the pedestal region was scaled by $C_J = 0.8$. The lines are sketches to indicate the location of the various sets of data points.

the TEQ equilibrium code [35] with the same q profile and discharge shape as in an original equilibrium reconstructed from the experimental data, but with the pressure profiles scaled by a factor that is constant as a function of radius. For each new equilibrium, the $n = 1$ stability was calculated using the DCON code [36] and the scale factor was iterated to find a marginally stable equilibrium. The original equilibrium is the best fit [21, 26] to poloidal field and flux measurements, the measured temperature and density profiles, and local measurements of the magnetic field pitch angle from the motional Stark effect (MSE) diagnostic. For these discharges, MSE measurements provide constraints on the equilibrium reconstruction across the majority of the plasma radius, but data were not available with resolution sufficient to resolve the local current density peak in the pedestal region (e.g. figure 2 at $\rho > 0.8$). Instead, the J profile in the pedestal region was constrained during the reconstruction to match the profile predicted by a time-dependent simulation executed as described in section 3.

If the J constraint in the pedestal is set to 100% of the current density predicted by the simulation, the χ^2 goodness of fit of the reconstruction to the measurements can be significantly higher than if the constraint values are scaled by a factor $C_J < 1$. (The pressure profile data provided as input
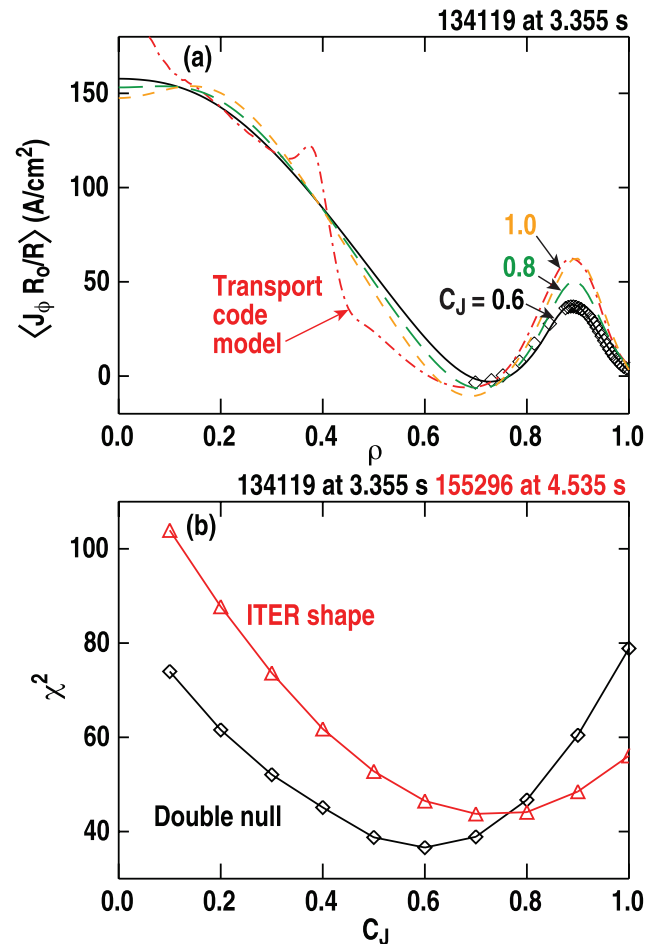
Figure 11. (*a*) The reconstructed toroidal current density profile for three different values of C_J for the discharge in figures 3(*a*)–(*c*) at 3.355 s: 0.6 (solid line), 0.8 (long-dash line), 1.0 (dashed line). The diamonds show the current density constraints for the $C_J = 0.6$ case. The dot-dash curve is the current density profile predicted by the transport code simulation. (*b*) χ^2 of the equilibrium reconstruction as a function of C_J for the discharge in figures 3(*a*)–(*c*) at 3.355 s (black) and the discharge in figure 7 at 4.535 s.

to the fitting procedure are held fixed as C_J is changed.) For instance, figure 11(*a*) shows the changes in the reconstructed current density profile as C_J is varied along with an example of the current density constraints. The value of χ^2 varies with C_J by a factor of two with the minimum at $C_J \approx 0.6$ in this case (diamonds, figure 11(*b*)). The optimum value of C_J depends on the discharge conditions. For the figure 3(*a*)–(*c*) discharge, the optimum value of C_J varies during the discharge, from 0.5 during the β_N ramp-up to 0.8 at the end of the discharge, a behavior that is typical of the highest β_N discharges in the double-null shape. In the ITER shape discharge (figure 7), the optimum C_J is more constant at ≈ 0.8 and the increase in χ^2 is smaller as C_J is increased (triangles, figure 11(*b*)).

These results indicate that the poloidal field, poloidal flux, pressure profile, and MSE measurements in these high β_N, high ℓ_i discharges are most consistent with less current density in the pedestal region than is predicted by the models. The reason for this is not clear, as low equilibrium reconstruction χ^2 for $C_J = 1$ has generally been observed previously [37]. It is
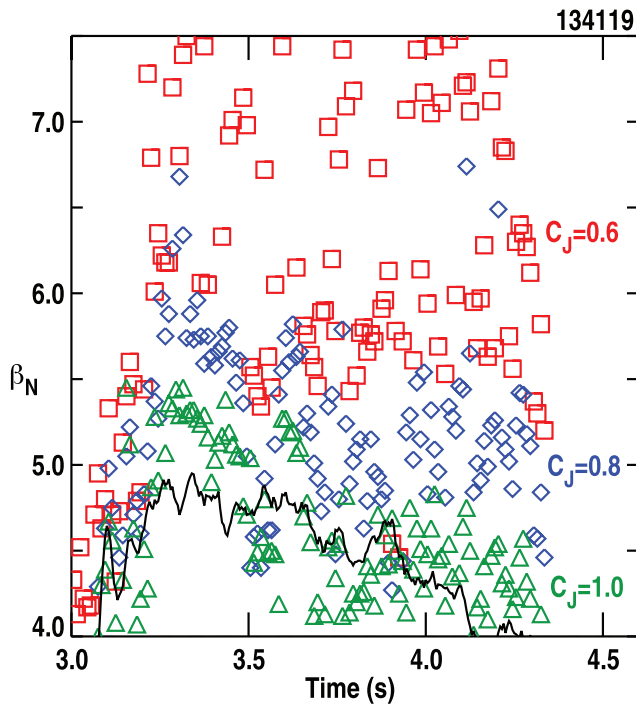
Figure 12. The ideal MHD $n = 1$ stability limit calculated including the conducting vacuum vessel wall for the discharge shown in figure 3(*a*)–(*c*) for three different values of C_J: 0.6 (squares), 0.8 (diamonds) and 1.0 (triangles). The solid line is the β_N in the experiment.

Figure 13. Measured pressure peaking factor $f_p = P(0)/\langle P \rangle$ for the double-null divertor shape discharge shown in figures 3(*a*)–(*c*) (diamonds) and the ITER shape discharge shown in figure 7 (triangles). The H-mode transition time shown is only for the double-null shape discharge, the transition in the ITER shape discharge occurred before the initial time shown on the plot.

possible that discrepancies between the model and the experiment are simply more prominent in these high poloidal beta (β_P) discharges [38]; in the figure 3 discharges, $\beta_P > 3$. The differences between the model and the experiment could be in the J_{IND} and/or J_{BS} profiles. With a significant negative surface voltage, J_{IND} can be large in the pedestal region, and the surface voltage simulation and measurement can differ, particularly at the beginning of the high β_N phase (figure 4(*a*)). The bootstrap current model used here [27, 28] agrees well for these discharges with the first-principles kinetic model implemented in the NEO code [39], so the discrepancy between experiment and model is not a result, for instance, of over prediction of J_{BS} at high collisionality [40] as found for other high β_P DIII-D discharges [38].

The predicted β_N at the ideal, with-wall $n = 1$ stability limit decreases if the pedestal region constraint on J for the equilibrium reconstruction is increased. For the figures 3(*a*)–(*c*) discharge, β_N at the calculated limit varies over a range of about 20–40% as C_J is varied between 0.6 and 1.0 (figure 12). With $C_J = 1.0$, the experimental discharge has β_N close to the calculated stability limit. With reduced pedestal J, though, to be more consistent with the measurements used in the equilibrium reconstruction, the stability limit is ≈15–30% above the experimental β_N. In particular, early in the high β_N phase (3–3.3 s), where the C_J that minimizes χ^2 is 0.5–0.6, the calculated stability limit is $\beta_N > 6$. Other features of the stability limit analysis can also modify the predicted stability limit, including the method of scaling the pressure profile from the original equilibrium reconstruction, the treatment of the separatrix flux surface when increased β_N equilibria are produced,
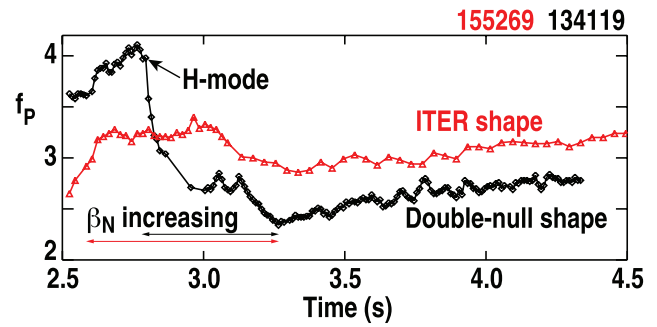
and features of the shapes of the pressure and current profiles that tend to produce scatter in the stability limit result (in particular, for example, the $C_J = 0.6$ results in figure 12).

The stability limits can be high, $\beta_N > 5$, in these discharges because of the increased values of ℓ_i and also because the plasma pressure profiles are relatively broad, as indicated by low values of the pressure peaking factor $f_p = P(0)/\langle P \rangle$ (figure 13). Previous work, both experimental and theoretical, has demonstrated the importance of a broad pressure profile in achieving high β_N limits [14, 41]. Modeling [41] has shown that with $f_p \leqslant 2.5$, similar to the lowest values in figure 13, the ideal low-n stability limit can exceed $\beta_N = 4$ even in high q_{min}, low ℓ_i discharges. In figure 13, the initial rapid drop in f_p from above 4 for the double-null shape discharge is a result of the transition to H-mode, but following that, for both discharge shapes, there is a decrease in f_p that occurs during the β_N rise. The changes in the temperature and density profiles that result in the decrease in f_p are shown in figure 14 for the double-null shape discharge. Much of the decrease in f_p occurs because of an increase in the pedestal density and a flattening of the density profile ($3.2 < \beta_N < 4.6$, figure 14(*a*)). There is also a broadening of the temperature profiles that is most evident from the increase at mid-radius, $\rho \approx 0.5$, when the density profiles are relatively constant ($\beta_N = 4.6, 4.9$) (figures 14(*b*) and (*c*)). This is consistent with reference [21] where a broadening of the core pressure profile and a corresponding decrease in f_p as a result of an increase in β_N is documented for discharges with a wide range of q profiles. The gradual increase in f_p during the high β_N phase (figure 13) could be accounted for by the decreasing β_N. In the ITER-shape discharge, though, β_N is relatively constant while f_p increases, indicating a possible role of changes in the core magnetic shear profile shape as ℓ_i decreases. The overall higher f_p in the ITER-shape case could indicate a dependence on the discharge shape, but the differences likely result from lower β_N. The lower calculated stability limits for the ITER-shape discharge (figure 10) are expected as a result of the changes in both the shape and f_p.

In the discharges with $n = 3$ fields applied (figure 8), the values of both ℓ_i and f_p play a role in determining the β_N
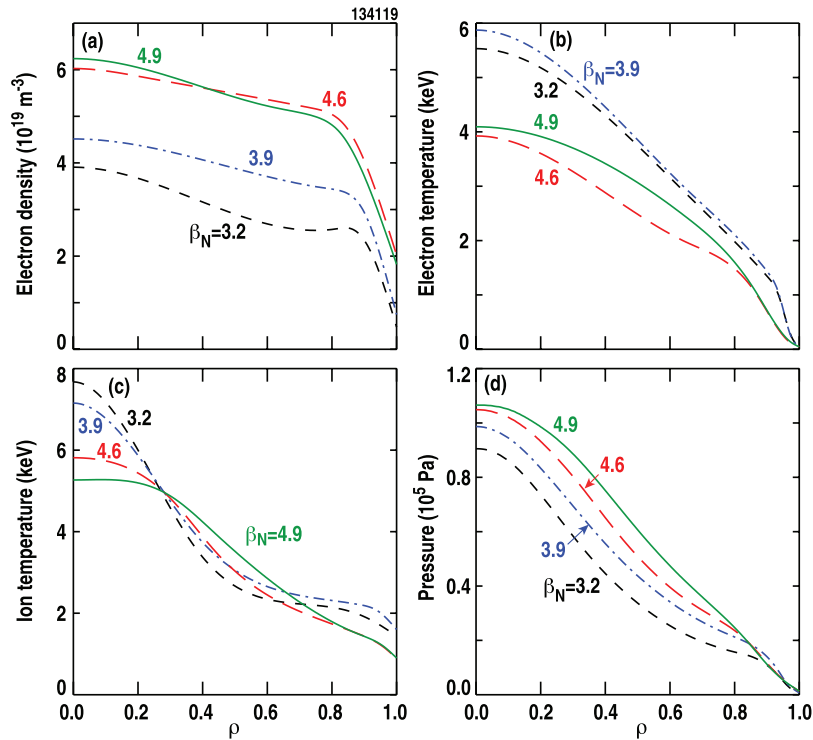
Figure 14. Parameter profiles at four different times during the rise in β_N in the discharge shown in figures 3(*a*)–(*c*): 2.905 s, $\beta_N = 3.2$, $f_p = 3$ (dashed), 3.005 s $\beta_N = 3.9$, $f_p = 2.7$ (dot–dashed), 3.165 s $\beta_N = 4.6$, $f_p = 2.6$ (long dashes), 3.275 s $\beta_N = 4.9$, $f_p = 2.4$ (solid).

stability limit. The two cases with the highest I coil current have a significantly increased f_p (figure 15(*b*)) as a result of both increased pressure on axis and decreased H-mode pedestal pressure. This change in f_p is reflected in a reduction in the calculated ideal-wall stability limit (figure 15(*a*)). The no-wall stability limit, however, shows no dependence on the I coil current, possibly because the increase in f_p is offset by the increase in ℓ_i.

A variety of low *n* fluctuations is observed in these discharges, as illustrated by the frequency/mode number spectrum for the discharge shown in figures 3(*d*)–(*f*) (figure 16). Although $q_{min} \approx q(0)$ is near 1, sawtooth oscillations are only clearly present during the ohmic heating phase. After that, there are periods with continuous 1/1 oscillations with frequency corresponding to the toroidal rotation frequency at the magnetic axis (e.g. figure 16 prior to 2.8 s) and periods with fishbone-like bursts of 1/1 oscillation at similar frequencies. The fishbone-like bursts grow and decay in amplitude on roughly the same timescale. There are also 1/1 bursts with a gradual growth in amplitude followed by a rapid collapse, similar to an internal kink-like sawtooth precursor. In figure 16, this type of burst immediately precedes the onset of the continuous 2/1 tearing mode. In a large fraction of the discharges where a 2/1 mode occurs, the mode onset immediately follows a fishbone-like or internal kink-like 1/1 burst. During discharges aimed at determining the highest achievable β_N, a 2/1 tearing mode that occurs during the β_N rise sets the maximum β_N at 3.8–4 in the scaled ITER shape and at $\beta_N > 5$ in the double-null discharge shape (e.g. figures 3(*d*)–(*f*)).

There has been some success in avoiding the 2/1 mode, even with β_N near 5, with the ECCD deposition profile
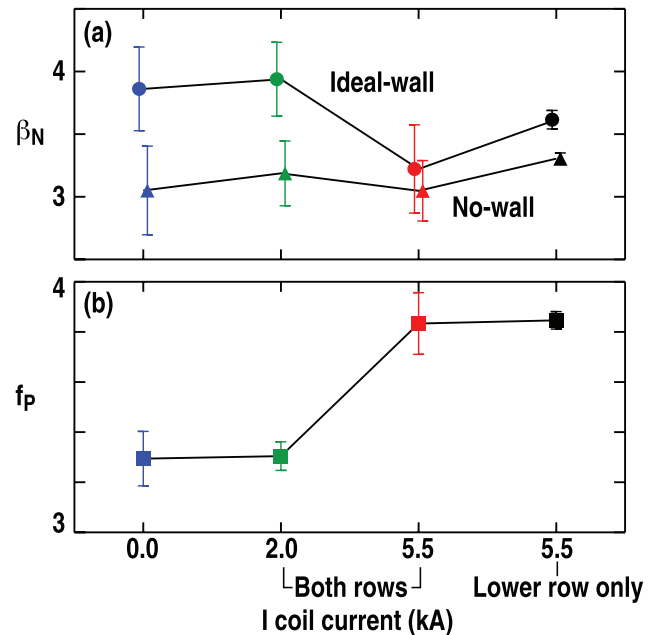
Figure 15. Parameters averaged over the interval 3–4 s for the discharges shown in figure 8. (*a*) Ideal $n = 1$ MHD stability limits calculated without the vacuum vessel wall (triangles) and with the vessel wall (circles). For all four discharges, the reconstructed equilibria were computed with $C_J = 1$. (*b*) Pressure peaking factor, $f_p = P(0)/\langle P \rangle$. The error bars show the standard deviation. The data point colors match the colors of the curves in figure 8.

modified to be at or near the $q = 2$ surface (instead of at $\rho \approx 0.4$ as described in section 2). For instance, in the discharge shown in figure 17, the 2/1 mode appears only after a decrease in the ECCD power. In other cases, the mode
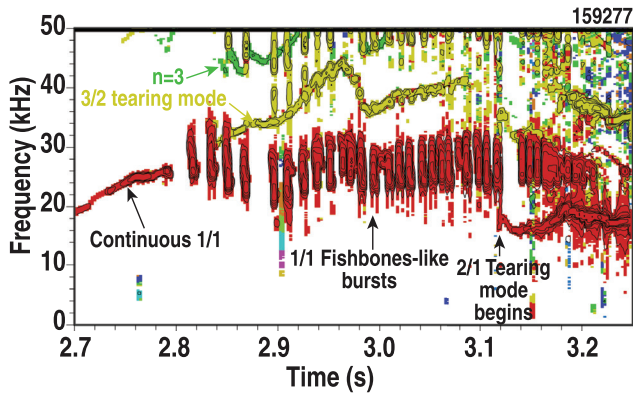
Figure 16. Time evolution of the frequency and mode spectrum of poloidal field fluctuations measured at the low-field-side vacuum vessel wall for the discharge shown in figures 3(*d*)–(*f*). Red: $n = 1$, yellow: $n = 2$, green: $n = 3$.

appears after the ECCD power is turned off. With 3.4 MW ECCD power applied throughout the high β_N phase, the onset of the 2/1 mode was completely avoided, or delayed until late in the discharge, $t > 4.5$ s, following a period of evolution of the current density profile. The DIII-D capability to use real-time motion of the mirrors in the EC power transmission system in order to maintain the deposition location in relation to the $q = 2$ surface [42] was employed in these experiments (figure 17(*b*)). In the case shown in the figure, the peak in J_{ECCD} was maintained close to the $q = 2$ surface at $\rho \approx 0.52$, but the EC-driven current was located in a relatively broad region, $0.4 < \rho < 0.6$. In a different discharge with the $q = 2$ surface still at $\rho \approx 0.52$, the EC power deposition was shifted to the region $0.33 < \rho < 0.52$ and the 2/1 mode avoidance was equally effective. Therefore, in these discharges the avoidance mechanism is likely related to modification of the temperature, density, rotation and/or current density profiles [43] rather than direct stabilization through replacement of J_{BS} at the rational surface which requires a narrow deposition profile at the $q = 2$ surface [44].

The timing of the H-mode transition was found to be a key to maintaining stability during the stored energy rise in order to access $\beta_N > 4$ and to allow operation at low q_{95}. If the H-mode transition is delayed until after the start of the high power beam heating phase (≈ 2.8 s), the first ELM can have a large impact on the stored energy. In the figures 3(*a*)–(*c*) case, for example, the first ELM follows a rapidly growing 1/1 kink-type mode (figure 18), and results in a rapid drop in β_N of about 0.6 and a rapid increase in the line average electron density. This event occurs with $\beta_N \approx 4$, below the maximum value. This discharge with $q_{95} \approx 7$ recovered from this event, but in some discharges with $q_{95} \approx 7$ and all discharges with lower q_{95}, either a 2/1 tearing mode or a disruption follows immediately. An increase in n_e of about 30% during the ohmic phase results in a H-mode transition during the period of the discharge with only EC heating (figure 7). A series of small ELMs follows this transition, and the impact of the first few ELMs after the start of high power neutral beam heating is reduced, allowing operation at lower q_{95}.
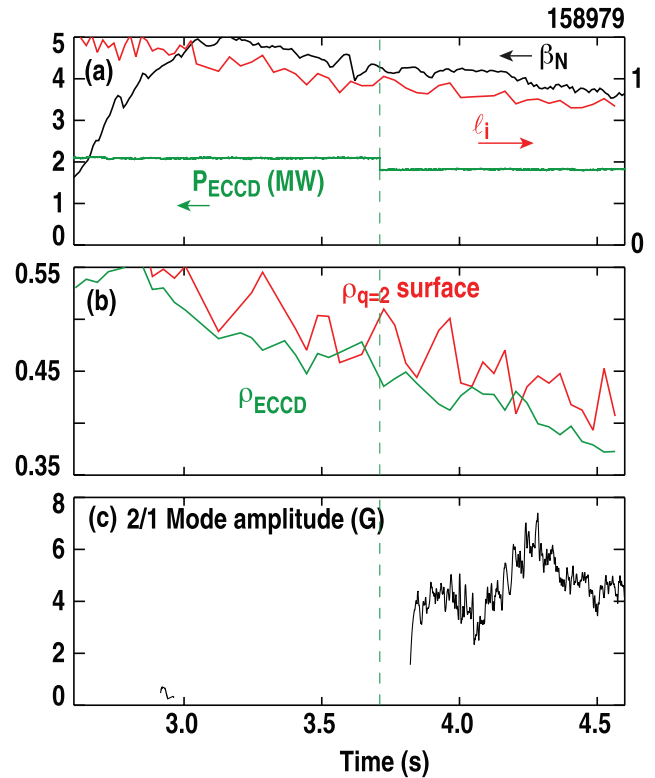

Figure 17. The time evolution of parameters of a discharge with ECCD deposited at the $q = 2$ surface. (*a*) Normalized pressure, internal inductance and ECCD power. (*b*) The normalized radii of the peak of J_{ECCD} and the $q = 2$ surface determined from a equilibrium reconstruction using poloidal field and flux measurements and motional Stark effect diagnostic data. (*c*) Amplitude of the 2/1 mode from mode analysis using the EIGSPEC [45] code to differentiate from a low amplitude 3/1 mode present prior to the onset of the 2/1 mode.

6. Modeling of a stationary high ℓ_i discharge for DIII-D

Modeling has been used to show that parameters for stationary, high ℓ_i, fully noninductive operation are attainable in DIII-D with an increase in the available heating and current drive power. Two key issues were evaluated: (1) the effect of the H-mode pedestal current density on the attainable ℓ_i and the β_N limit and (2) the power and configuration required for the external heating and current drive.
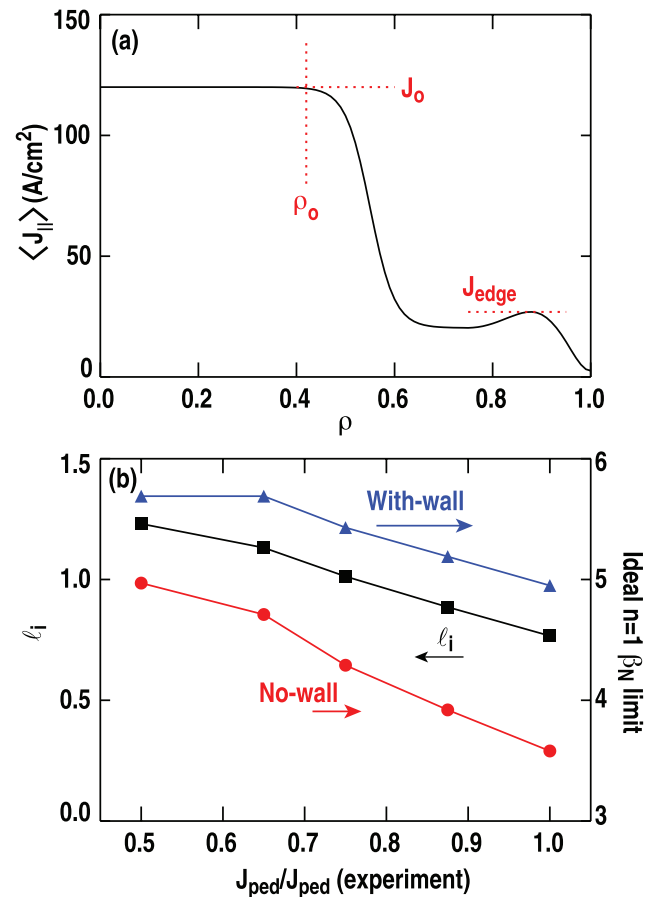
The effect of the pedestal current density was studied using model equilibria with a J profile in the shape that is optimum for achieving high ℓ_i. As shown in figure 19(*a*), the current density is modeled as uniform with value J_0 in a region $0 < \rho < \rho_0$. J_0 was chosen to set $q(0) = 1.01$ and ρ_0 was chosen in order to set q_{95}. The required ρ_0 increases from 0.3 at $q_{95} = 7.5$ to 0.45 at $q_{95} = 4.5$ (with B_T held constant) in order to accommodate the increased plasma current. The plasma shape, pressure profile shape, with $f_p = 2.7$, and the J_{BS} profile (with $C_{BS} = 1$) in the H-mode pedestal region are taken from the double-null divertor shot in figures 3(*a*)–(*c*) at 3.625 s. A series of equilibria was created with J_{edge} (figure 19(*a*)) equal to varying fractions of the experimental pedestal-region
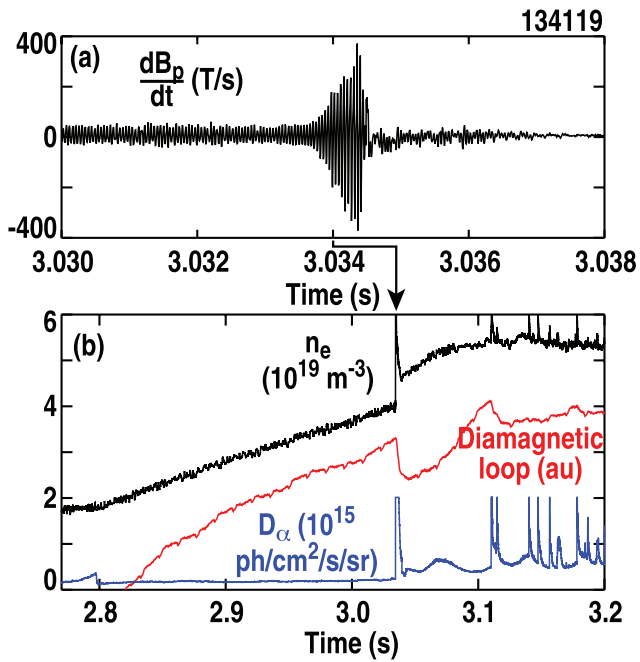
Figure 18. Time evolution at the end of the ELM-free phase in the discharge shown in figures 3(*a*)–(*c*). (*a*) Poloidal field fluctuations on an expanded timescale, (*b*) line average electron density, the diamagnetic loop signal (which provides a high time resolution diagnostic that is proportional to the stored energy) and the divertor D_α light emission. Spikes in D_α indicate occurrence of an ELM.


Figure 19. (*a*) The shape of the *J* profile, optimized for achieving high ℓ_i, that was used to produce the model equilibria that were used to assess the effect of the pedestal current density. (*b*) From model equilibria, parameters as a function of the assumed height of the *J* peak in the H-mode pedestal region: ℓ_i at $\beta_N = 4.5$ (squares), and the ideal $n = 1$ stability limits with (triangles) and without (circles) the stabilizing effect of an ideal wall at the location of the DIII-D vacuum vessel. In all cases, $B_T = 1.75\,T$, $q_{95} = 6.5$.

J_{BS}. As J_{edge} was reduced to half the experimental value, ℓ_i increased from ≈ 0.75 to ≈ 1.3 (figure 19(*b*)). The calculated stability limits show the expected increase with ℓ_i, reaching ≈ 5 for the no-wall limit and ≈ 6 for the ideal-wall limit. There is thus a significant advantage in stability if current density can be shifted from the pedestal region to the core. These β_N limit values are similar to those calculated for the double-null shape discharge (figure 10).

Transport code studies were used to explore how increased current drive and heating powers similar to those in a proposed DIII-D upgrade (13 MW off-axis neutral beam, 9 MW ECCD at 110 GHz) could be applied to maintain a stationary, $f_{NI} = 1$ high ℓ_i discharge. The FASTRAN framework [46] was used to calculate a stationary current density profile solution using the bootstrap current and current drive models referenced in section 3, and the TGLF transport model [47] to predict the temperature profiles. The full electron density profile was taken from the figures 3(*a*)–(*c*) discharge at 3.625 s, as were the electron and ion temperature profiles in the region $\rho > 0.8$. These electron and ion temperature profiles were scaled to adjust J_{edge} to be 75% of the J_{BS} predicted by the model for the for the original experimental profiles, setting the boundary condition for the TGLF temperature profile prediction. The fraction of the experimental J_{BS} was selected for this initial modeling study from figure 19(*b*) so that ℓ_i would be approximately 1, motivated by the 'optimized high ℓ_i' equilibrium discussed in reference [15]. The accessible current density and pressure profiles were studied by varying the current drive and heating powers, the deposition profiles for the ECCD sources, and the relative fractions of on-axis and off-axis

neutral beam powers. The goal was to maximize the stationary value of β_N consistent with the calculated stability limits and the required current drive power (which is also the heating power). The result from this initial modeling study is slightly overdriven, with $\ell_i = 1.07$, $\beta_N = 4$, $f_{BS} = 0.5$, $f_{NBCD} = 0.35$, $f_{ECCD} = 0.3$, $H_{89} = 2.3$, $H_{98(y,2)} = 1.1$, and the ideal $n = 1$ stability limits $\beta_N \approx 4.1$ without a conducting wall and $\beta_N = 4.84$ with a wall. The ECCD current drive efficiency [48], using on-axis parameters, is $\eta = (e^3/\epsilon_0^2)(n_e I_{ECCD} R)/(P_{ECCD} k T_e) = 0.19$, or 0.037 A/W. The bootstrap current density profile is broad (figure 20) and both on-axis and off-axis neutral beam current drive coupled with ECCD close to the axis are used to generate the current density peak extending to $\rho \approx 0.4$ that maintains the increased value of ℓ_i. All of the available off-axis neutral beam power is used in order to broaden the fast ion pressure profile as much as possible in order to reduce f_p. The off-axis neutral-beam-driven current density is minimized, though, through choice of the toroidal field direction [49]. A similar solution requiring additional input power to reach higher $\beta_N \approx 5$, close to the ideal-wall stability limit, was also studied [50].
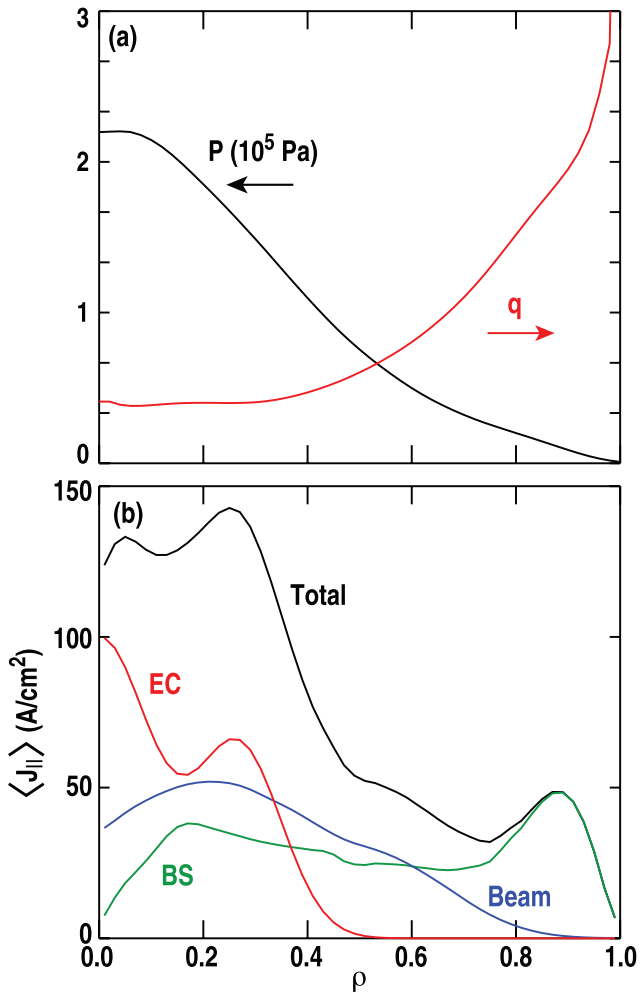
Figure 20. Profiles in the $\beta_N = 4$ transport code-modeled steady-state solution for DIII-D. (*a*) safety factor and pressure, (*b*) current densities. $B_T = -2$ T, $I_p = 1.1$ MA, $q_{95} = 6$, total injected neutral beam power is 20 MW with 13 MW injected off axis, and the ECCD power is 9 MW.

7. Conclusions

In this report, we have described the use of experiment and modeling to assess how a high ℓ_i scenario can be implemented for steady-state tokamak operation. The significant advantages of high ℓ_i operation that motivate this work are reflected in the experimental results, with discharges produced at very high $\beta_N \approx 5$ and with excellent confinement $H_{98(y,2)} \approx 1.8$. High ℓ_i operation is presently the only method to access β_N this high in conventional aspect ratio tokamaks, although stable access to $\beta_N = 5$ has been projected for a future scenario with $q_{min} > 2$ and a very broad J profile that can maximize the stabilizing effect of the conducting wall [51]. The $n = 1$ ideal stability limits calculated using the measured plasma parameters were shown to be higher than the experimental β_N, with broadening of the pressure profile with increasing β_N playing an important role in raising the stability limit along with the elevated values of ℓ_i. It was shown that there is uncertainty, though, in the calculated stability limits because of sensitivity to the current density in the H-mode pedestal region, which

is not well diagnosed. The highest β_N, double-null divertor, relatively high q_{95} discharge had total noninductively driven current more than sufficient for steady-state operation, with a reduction in q_{95} required in order to reduce f_{NI} to 1 at the same β_N. In the ITER-shape discharges where q_{95} was lower, higher β_N is required in order to reach $f_{NI} = 1$. A relatively simple method to create the high β_N, high ℓ_i discharge was described that could be used to implement a high ℓ_i scenario for steady-state operation in future, larger tokamaks.

Continued development of a high ℓ_i steady-state scenario requires work in several areas, perhaps most important of which is to determine how the H-mode pedestal can be maintained with appropriate pressure and current density. The observed time evolution of ℓ_i in the experiment and the study of model equilibria have shown that the pedestal J in the highest β_N discharges is too high to be compatible with stationary $\ell_i > 1$. Application of a $n = 3$ perturbing magnetic field was shown to decrease the pedestal J with a corresponding increase in ℓ_i, but the accompanying reduction in the pedestal pressure resulted in increased pressure peaking and reduced stability limits. Ideally, the H-mode pedestal would be operated in a regime with both high pressure and low current density. The highest β_N discharges reported here have relatively high $q_{95} \approx 7.5$, and in order to attain the high values of β_T required for a reactor, q_{95} must be reduced. A reduction in q_{95} would be expected to reduce the fraction of I_p that results from bootstrap current in the pedestal region as a result of both a reduction of the pedestal width at lower β_P [52] and the scaling of the bootstrap current fraction with q_{95} [21].

The stability-limiting mode in the high ℓ_i scenario is the $n = 1$ tearing instability, also a feature of other tokamak operating regimes [43, 53, 54]. The onset of a $n = 1$ mode near the ideal stability limit, such as in the figures 3(*d*)–(*f*) discharge, may be a result of rapidly decreasing tearing mode stability as the ideal stability limit is approached [43, 55]. However, in some cases the $n = 1$ mode limits β_N to a value below the no-wall stability limit, as in the figure 7 discharge. Therefore, continued work on optimizing the plasma profiles to avoid this mode is required, with ECCD one of the key available tools.

Finally, development of the capability to provide the required externally-driven current near the axis is needed in order to be able to operate high ℓ_i discharges in a stationary, rather than the present transient, manner. The modeling study showed that current drive power above what is presently available at DIII-D is required, but that the planned power upgrades are suitable. Particularly important would be an increase in the ECCD power which can be used to efficiently provide a large fraction of the required current density in the region closest to the axis. Neutral beams also provide useful current drive even though the profile of the driven current is rather broad. As shown in the study of model equilibria, the J profile for high ℓ_i still has a relatively broad central region of high J. A method to mitigate the limitations on $J(0)$ imposed by the sawtooth instability [56] would allow external current drive closer to the axis, increasing efficiency and also providing access to higher values of ℓ_i.

Acknowledgments

References

[1] Zarnstorff M.C. *et al* 1991 *Proc. 13th Int. Conf. Plasma Phys. Control. Fusion Res.* (*Washington, DC, 1–6 October, 1990*) vol 1 (Vienna: IAEA) p 109

[2] Murmann H., Stroth U., ASDEX-Team and NI-Team 1991 *Proc. 18th Eur. Conf. Control. Fus. Plasma Phys. (Berlin, Germany, 3–7 June, 1991)* vol 15C p 109

[3] Strait E.J. *et al* 1991 *Proc. 18th Eur. Conf. Control. Fus. Plasma Phys. (Berlin, Germany, 3–7 June, 1991)* vol 15C p 105

[4] Sabbagh S.A. *et al* 1991 *Phys. Fluids* B **3** 2277

[5] Challis C.D. *et al* 1992 *Nucl. Fusion* **32** 2217

[6] Kamada Y. *et al* 1993 *Nucl. Fusion* **33** 225

[7] Ferron J.R. *et al* 1993 *Phys. Fluids* B **5** 2532

[8] Lao L.L. *et al* 1993 *Phys. Rev. Lett.* **70** 3435

[9] Hoang G.T. *et al* 1994 *Nucl. Fusion* **34** 75

[10] Fredrickson E.D. *et al* 1997 *Phys. Plasmas* **4** 1589

[11] Lao L.L. *et al* 1998 *Phys. Plasmas* **5** 1050

[12] Urano H. *et al* 2009 *Nucl. Fusion* **49** 095006

[13] Yushmanov P.N., Takizuka T., Riedel K.S., Kardaun O.J.W.F., Cordey J.G., Kaye S.M. and Post D.E. 1990 *Nucl. Fusion* **30** 1999

[14] Howl W. *et al* 1992 *Phys. Fluids* B **4** 1731

[15] Lin-Liu Y.R. *et al* 1999 *Phys. Plasmas* **6** 3934

[16] Lao L.L. *et al* 1992 *Phys. Fluids* B **4** 232

[17] Najmabadi F. *et al* 2006 *Fusion Eng. Design* **80** 3

[18] Turnbull A.D. *et al* 1998 *Nucl. Fusion* **38** 1467

[19] Mikkelsen D.R. 1988 *Phys. Fluids* B **1** 333

[20] Ferron J.R. *et al* 2006 *Nucl. Fusion* **46** L13

[21] Ferron J.R. *et al* 2011 *Nucl. Fusion* **51** 063026

[22] Humphreys D.A. *et al* 2009 *Nucl. Fusion* **49** 115003

[23] Snipes J.A. *et al* 2012 *Fusion Eng. Design* **87** 1900

[24] ITER Physics Expert Group on Confinement, Transport, Confinement Modeling, Database and ITER Physics Basis Editors 1999 *Nucl. Fusion* **39** 2175

[25] St John H.E., Taylor T.S., Lin-Liu Y.R. and Turnbull A.D. 1995 *Proc. 15th Int. Conf. Plasma Phys. Control. Nuc. Res*. (*Seville, Spain*, 26 September–1 October, 1994) (Vienna: IAEA) p 603 (www-naweb.iaea.org/napc/physics/FEC/STIPUB948_VOL3.pdf)

[26] Lao L.L., Ferron J.R., Groebner R.J., Howl W., St John H., Strait E.J. and Taylor T.S. 1990 *Nucl. Fusion* **30** 1035

[27] Sauter O., Angioni C. and Lin-Liu Y.R. 1999 *Phys. Plasmas* **6** 2834

[28] Sauter O., Angioni C. and Lin-Liu Y.R. 2002 *Phys. Plasmas* **9** 5140

[29] Pankin A., McCune D., Andre R., Bateman G. and Kritz A. 2004 *Comput. Phys. Commun.* **159** 157

[30] Lin-Liu Y.R., Chan V.S. and Prater R. 2003 *Phys. Plasmas* **10** 4064

[31] Groebner R.J. and Osborne T.H. 1998 *Phys. Plasmas* **5** 1800

[32] Poli F.M. *et al* 2014 *Nucl. Fusion* **54** 073007

[33] Evans T.E. *et al* 2006 *Phys. Plasmas* **13** 056121

[34] Miller R.L. *et al* 1997 *Phys. Plasmas* **4** 1062

[35] Lodestro L.L. and Pearlstein L.D. 1994 *Phys. Plasmas* **1** 90

[36] Glasser A.H. and Chance M.S. 1997 *Bull. Am. Phys. Soc.* **42** 1848

[37] Thomas D.M. *et al* 2005 *Phys. Plasmas* **12** 056123

[38] Ren Q. *et al* 2015 *Plasma Phys. Control. Fusion* **57** 025020

[39] Belli E.G. *et al* 2008 *Plasma Phys. Control. Fusion* **50** 095010

[40] Belli E.G. *et al* 2014 *Plasma Phys. Control. Fusion* **56** 045006

[41] Ferron J.R. *et al* 2005 *Phys. Plasmas* **12** 056126

[42] Kolemen E. *et al* 2014 *Nucl. Fusion* **54** 073020

[43] Turco F. *et al* 2012 *Phys. Plasmas* **19** 122506

[44] Petty C.C. *et al* 2004 *Nucl. Fusion* **44** 243

[45] Olofsson K.E.J. *et al* 2014 *Plasma Phys. Control. Fusion* **56** 095012

[46] Park J.M. *et al* 2010 *Proc. 23rd Int. Conf. Fusion Energy* (*Daejeon, Korea, 10–16 October 2010*) (Vienna: IAEA) EXC/P2-05 www.naweb.iaea.org/napc/physics/FEC/FEC2010/html/index.htm

[47] Staebler G.M., Kinsey J.E. and Waltz R.E. 2007 *Phys. Plasmas* A **14** 055909

[48] Luce T.C. 1999 *Phys. Rev. Lett.* **83** 4550

[49] Murakami M. *et al* 2009 *Nucl. Fusion* **49** 065031

[50] Park J.M. *et al* 2015 *Phys. Plasmas* to be submitted

[51] Ferron J.R. 2013 *Phys. Plasmas* **20** 092504

[52] Groebner R.J. *et al* 2009 *Nucl. Fusion* **49** 085037

[53] Turco F. and Luce T.C. 2010 *Nucl. Fusion* **50** 095010

[54] Luce T.C. *et al* 2004 *Phys. Plasmas* **11** 2627

[55] Brennan D.P. 2003 *Phys. Plasmas* **10** 1643

[56] Igochine V. and 2015 *Active Control of Magneto-hydrodynamic Instabilities in Hot Plasmas* (Berlin: Springer) chapter 4